INSTITUTE OF PHYSICS PUBLISHING and INTERNATIONAL ATOMIC ENERGY AGENCY NUCLEAR FUSION

Nucl. Fusion **45** (2005) 531–536 doi:10.1088/0029-5515/45/6/016

Energy conversion in a reactor chamber for fast ignition heavy ion fusion

Yu.N. Orlov[1,a], M.M. Basko[2], M.D. Churazov[2], P.P. Ivanov[3], D.G. Koshkarev[2], S.A. Medin[3], A.N. Parshikov[3], B.Yu. Sharkov[2] and V.M. Suslin[1]

[1] Keldysh Institute for Applied Mathematics, RAS, Miusskaya 4, 125047 Moscow, Russia
[2] Institute for Theoretical and Experimental Physics, B.Cheremushkinskaya 25, 117259 Moscow, Russia
[3] Institute for High Energy Densities, RAS, Izhorskaya 13/19, 125412 Moscow, Russia

E-mail: orlmath@keldysh.ru

Received 10 December 2004, accepted for publication 4 April 2005
Published 26 May 2005
Online at stacks.iop.org/NF/45/531

Abstract
The concept of a power plant for a fast ignition heavy ion fusion is briefly reviewed. The reactor chamber response to x-ray irradiation, ion debris and neutron flux is considered. Ablation of a thin liquid film at the first wall is simulated by means of a one-dimensional hydrodynamic code. Ion debris reheating of the vaporized coolant is evaluated. Vaporization and subsequent condensation of the coolant is computed with the use of a kinetic model of fast condensation. Heating of the blanket due to neutron deposition and corresponding generation of pressure and stress waves are simulated by means of the Monte Carlo (MCNP) code and by the strength media mechanics code, respectively.

PACS numbers: 52.28.Hm, 28.52.Av, 52.57.Fg

1. Introduction

The principal aspects of DT-fusion based on heavy ion acceleration technologies are determined mainly by the two design factors: the type of target drive and the blanket structure. At the moment the most advanced concept HYLIFE-II [1, 2] employs the indirect drive of the target and the thick liquid wall of the blanket structure. The advantages of this concept are mitigation of problems at the driver–reactor-chamber interface and in chamber construction materials. The difficulties involved are the organization of a radiation-proof pocket of liquid jets and the demand of higher gain in target burn.

In [3, 4] an alternative concept of heavy ion fusion was proposed. In this concept the direct drive of the cylindrical target in the fast ignition mode and thin liquid wall design of the blanket are accepted.

This approach is characterized by a simple driver–reactor chamber interface and a moderate value of demanded gain. The problems with the fast ignition heavy ion fusion (FIHIF) concept are related to rigid physical conditions of the implementation of the fast ignition scenario and heavy ion driver length.

In this paper new data on x-ray interaction with the liquid film at the first wall and thermal and mechanical neutron impact on the blanket structure are given from computer simulation by means of the numerical codes developed.

The principal features of the FIHIF concept are described in [3, 4] and include a high power driver, cylindrical target and a reactor chamber with a thin liquid protection layer and large condensation vault.

The high power heavy ion accelerator is fed by ion sources for four Pt isotopes with plus and minus charge states, arranged in 8 groups of 4 devices each. In the main linac the ion energy is increased to 100 GeV. After this the ions with different charges and masses are separated into 8 beams, which are compressed in two stages: in storage rings and in exit sections by the time-of-flight method. The final summation of 8 beams in an individual transfer line results in a single bunch of 0.2 ns duration delivered to the compressed target. The average power, needed for acceleration of this ignition beam, equals 2×10^{15} W. The preliminary compression of the target is accomplished by the hollow beam, which carries only Pt^{+}_{192} ions. The compression beam is profiled having a peak power of 3.7×10^{14} W.

The repetition rate of the FIHIF driver is taken as 8 Hz, which provides 2 shots per second in each of 4 reactor chambers. The evaluated nominal driver efficiency is equal to 0.25.

The target presents a DT fuel cylinder with a radius of 0.112 cm and a length of 0.71 cm, which is surrounded by a lead

[a] Author to whom any correspondence should be addressed.

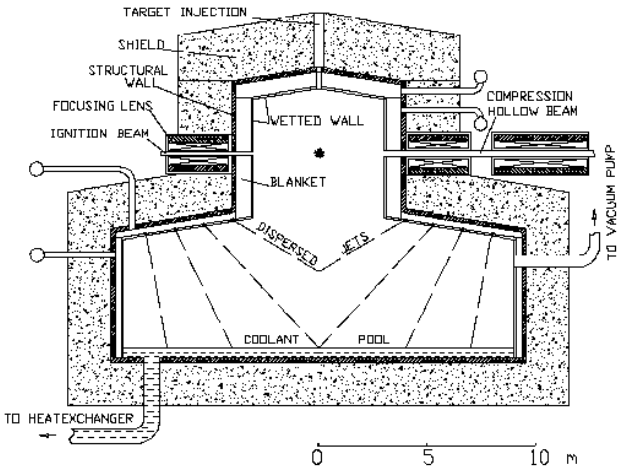

Figure 1. Reactor chamber for FIHIF power plant.

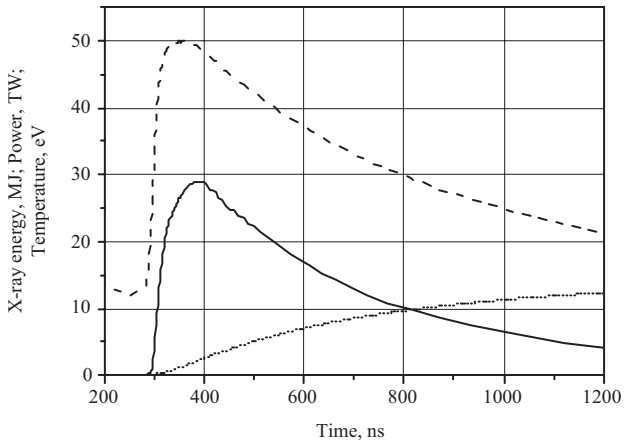

Figure 2. Temporal profiles of x-ray characteristics for the FIHIF cylindrical target. - - - -: temperature, ——: power, · · · · · ·: energy.

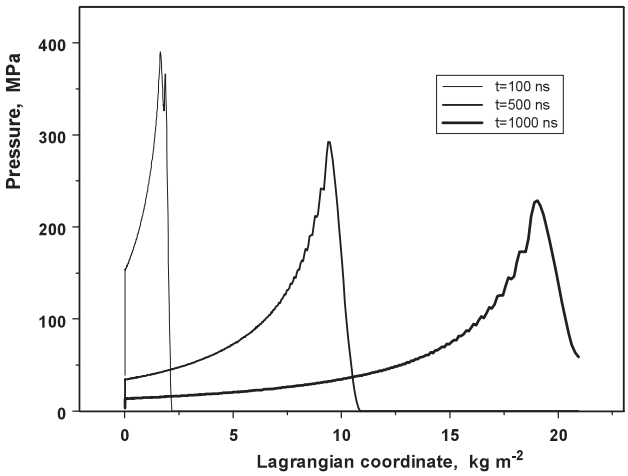

Figure 3. Shock wave propagation in the liquid film at the first wall.

shell with a radius of 0.4 cm and a length of 0.8 cm. The masses of fuel and lead are equal to 5.6 mg and 4.44 g, respectively. The length of the target is matched to the stopping range of 100 GeV Pt^{+}_{192} ions deposited by the compressing hollow beam.

The parameters of target compression and burn were determined successively in separate simulations [5]. The burn fraction amounts to 0.39 providing a fusion energy of 750 MJ and a gain of 100. This energy is partitioned among 580 MJ in neutrons, 154 MJ in debris and 17 MJ in x-rays.

The general design of the reactor chamber is shown in figure 1. The chamber consists of the two cylindrical sections: the upper smaller section in which the target explosion takes place and the lower section in which sprayed jets of coolant are injected. The diameters of the sections are 8 m and 16 m, respectively. Such a configuration prevents an overpressurization after the microexplosion and provides a high rate of vapour condensation on sprayed jets.

The coolant is eutectic $Li_{17}Pb_{83}$. The coolant temperature of the first wall film is taken as 823 K. A saturation density of vapour of $10^{18}\,m^{-3}$ corresponds to this temperature [6]. Under this condition the Pt ion beam is not deteriorated by an atmosphere in the reactor chamber.

The first wall and the blanket are of conventional design. The liquid film is formed at the SiC porous wall. In the blanket, the tubing is made of vanadium alloy. The structural wall is made of HT-9 steel.

The main problems under consideration are the behaviour of the liquid film under x-ray radiation and the dynamic response of the blanket to the neutron pulse.

2. Chamber response to x-rays and ion debris

X-ray radiation is originally absorbed by target material and then re-radiated by lead plasma. This causes the decrease of x-ray temperature and delay and lengthening of the x-ray pulse. In figure 2 the profile of the x-ray pulse is drawn according to [5]. The duration of the pulse is very long and exceeds 700 ns, the mean x-ray temperature is equal to 30 eV.

Interaction of x-ray radiation with the liquid film is simulated by the Lagrangian 1D-hydrodynamic code. This code solves equations of conservation of mass, momentum and energy, which include viscous friction, heat transfer and energy deposition of x-ray radiation. The latter is computed by means of the mass attenuation coefficient for eutectic $Li_{17}Pb_{83}$ determined with the use of individual substance data given in [7]. The wide-range equation of state is taken from [8] for lead; thus, the presence of lithium is neglected in thermodynamic properties. In the EOS the vaporization and the first ionization of lead is taken into account.

The data on the response of the $Li_{17}Pb_{83}$ liquid film to an x-ray radiation pulse are presented in figures 3–5.

The energy deposition of x-ray radiation occurs in the thin liquid layer at the first moments of time and later in vapour that expands from the liquid surface. This is accompanied by shock wave generation in the liquid film. In figure 3, we show the pressure profiles in liquid. In this figure, the shock wave spreads from the left side of the liquid film to the right side, i.e. from the explosion cavity to the first wall of the reactor chamber. The shock wave travels across the film with the velocity of sound, $2000\,m\,s^{-1}$. It crosses the film of 2 mm width in 1 μs and comes to the first wall with the amplitude of 250 MPa. The pressure in the tail of the pressure profile is equal to the saturation pressure at the vaporization front. It is seen that the saturation pressure decreases following the power

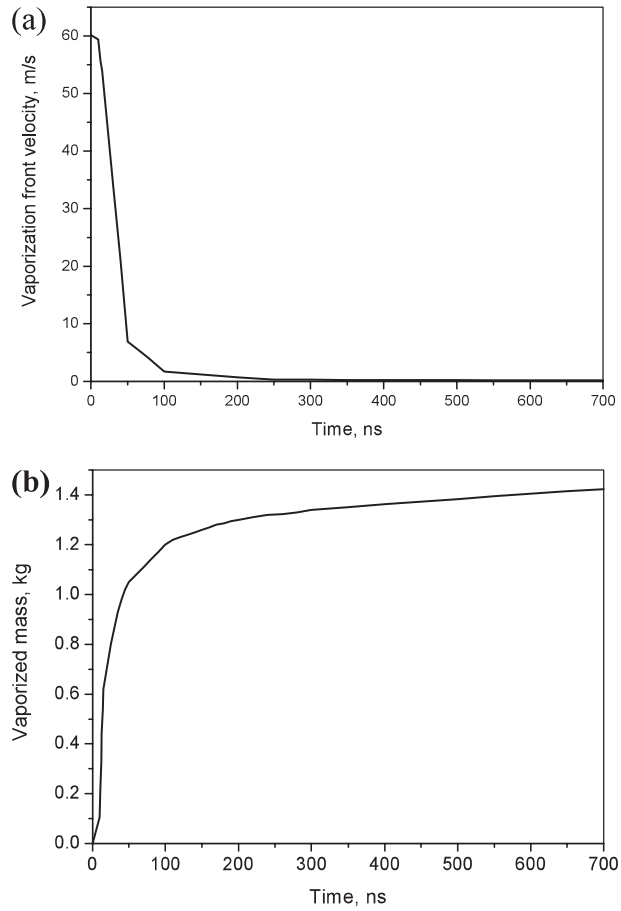

Figure 4. Vaporization front velocity (*a*) vaporized mass of liquid and total (*b*) versus time.

of x-ray radiation. The displacement of the vaporization front is small enough and is not seen in figure 3.

The velocity of the vaporization front and the total mass of vaporized liquid are shown in figure 4. The rate of vaporization falls substantially in 100 ns while energy deposition of x-ray radiation continues to rise. This is caused by the intensive absorption of x-ray radiation by vapour and demonstrates a screening effect of the vapour layer. The temperature and the density in this vapour layer are strongly non-uniform. There is a rarefied ionized external zone with a temperature of 3×10^6 K and a density of 10^{-6} kg m^{-3}.

In figure 5 the temporal variation of temperature at the vaporization front is presented. It decreases according to saturation pressure change. During the first 80 ns the vaporization occurs under the saturation curve. So the part of this graph exceeding the critical point of lead (6000 K), really does not belong to the saturation curve.

The saturation pressure at the liquid surface integrated in time determines the momentum transferred to the first wall due to the recoil effect. For the time interval of 1 μs we calculate that the impulse per unit area I amounts to 64 Pa c. We evaluate the first wall loading under impulse I using the solution of the problem of thin spherical shell oscillations in the case when the shell is surrounded by a liquid coolant [9]. Under conditions of the FIHIF blanket design the vibrations of the shell are aperiodic, i.e. the elastic strains are damped by the hydrodynamic coupling effect. In this case, the maximum

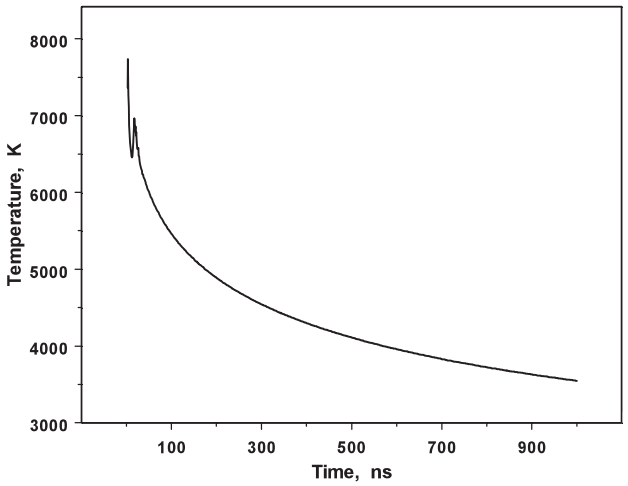

Figure 5. Vaporization front temperature versus time.

loading of the first wall is defined by the pressure at the first wall/coolant interface arising at the initial moment $p_0 = \rho_l c_l I / \rho_w \delta$, where $\rho_l c_l$ is the coolant impedance, ρ_w is the averaged density and δ is the thickness of the first wall and the liquid film. Taking the parameters of the liquid film and the first wall from tables 1 and 2 we obtain $p_0 = 20$ MPa. Taking into account that the proportional limit strength of the first wall is set as 35 MPa we conclude that the first wall works within the elastic range of the material state.

The expanding vapour layer starts to interact with the target debris flow at 10 μs, when 80 keV lead ions approach the first wall. According to the Bethe–Bloch formula for energy losses [10] the stopping range of lead ions equals 6×10^{-6} g cm^{-2}. This is much smaller than the mass width of the vapour layer. Therefore, it can be supposed that the debris ions are stopped in the vapour layer and the evaporated coolant is additionally reheated by debris ions. When the reheated vapour expands over the cavity of the reactor chamber, its evaluated resulting temperature and density amount to 230 eV (approximately equal to 2.5×10^6 K) and 1.5×10^{22} m^{-3}, respectively. The process of additional vaporization and consequent condensation is considered to start with these values of the initial parameters for the vapour.

We describe the evaporation–condensation processes by kinetic relationships [11] in the same way, as in [4]. We suppose, that droplets of dispersed jets in the lower chamber volume (see figure 1) provide the necessary area of the condensation surface (4.5×10^4 m^2 for droplets with a total mass of 7000 kg per shot). In figure 6 the temporal variation of vapour density is presented. It is seen that revaporization results in a density rise of one order of magnitude. The revaporization process is characterized by two distinguished phases. During 0.1 ms the temperature of ionized vapour rapidly decreases because of very intensive vaporization from the inner surface of the liquid film and droplets of dispersed jets. So, the thermal energy of vapour is diminished. At the moment of time of about 0.1 ms the condensation flow surpasses vaporization flow. The maximum mass of the evaporated coolant is 14 kg. The sharp decrease in vapour density after 1 ms is due to condensation on the dispersed jets after the time needed for uniform ionized vapour to spread throughout the chamber.

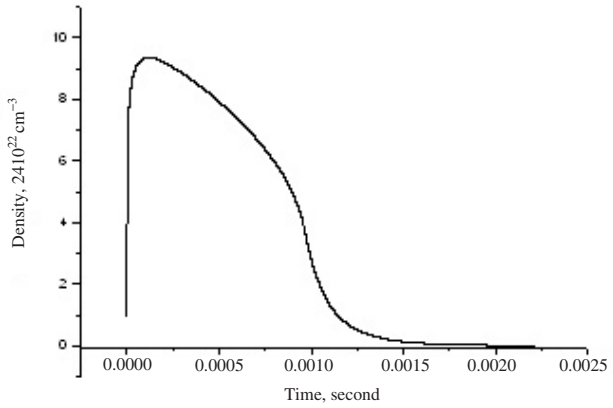

Figure 6. Temporal variation of vapour density in the reactor chamber after the shot.

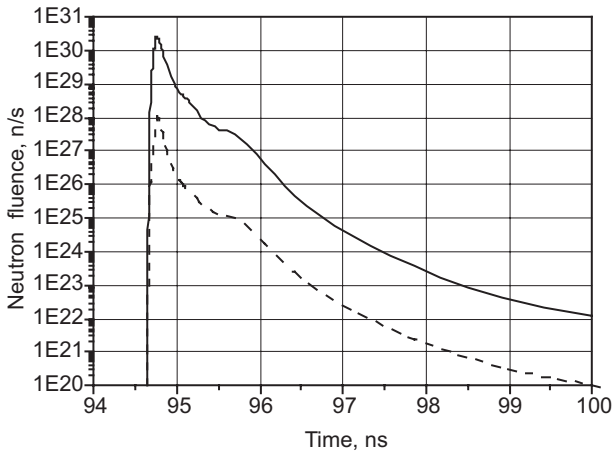

Figure 7. Neutron pulse of the FIHIF target microexplosion. ——: 14 MeV; - - - -: 2.45 MeV.

The vapour density practically reaches the saturation value at 0.01 s. This indicates that the condensation process would not limit the repetition rate of shots. Apparently, the actual limitation will be the rate of clean-up of liquid droplets. In the case of free gravity precipitation the repetition rate does not exceed 2 Hz.

One should note, that in spite of the short time of condensation, we cannot sufficiently decrease the mass of dispersed jets in the lower volume of the chamber. Since the difference between inlet and outlet coolant temperature is 200°, the energy accumulated by these jets and the liquid film, can be estimated from the coolant specific heat capacity (about 200 J kg^{-1} K^{-1}): this energy does not exceed the energy of x-ray and debris (170 MJ). So the total mass of film and jets cannot be less than 8500 kg and the mass of jets is about 6500–7000 kg.

3. Neutron heating of the blanket

The neutron pulse, generated in the DT-reaction, is presented in figure 7 according to [5].

The neutron spectrum is evaluated by stationary calculations with the use of the MCNP code [12] in the spherical approximation for the moment of central peaking of the neutron pulse. The average neutron energy is equal to 12.2 MeV. Two-dimensional calculations of neutron transport in the blanket with the use of the MCNP code resulted in a high value of the energy release in the materials. The tritium breeding ratio (TBR) for this blanket is equal to 1.112, and the blanket multiplication factor is evaluated as 1.117. So the total energy release per shot is equal to 818 MJ.

The blanket is presented by a multi-layer cylinder, the structure of which is given in table 1. The blanket thickness is equal to 52 cm. We enumerate blanket zones and inner radii from the surface of the liquid protecting layer.

Neutron heating generates a pressure/stress pulse, which travels across the blanket and refracts at the contact surfaces. For the evaluation of material loading we solve 1D hydrodynamic equations in cylindrical geometry. The computational interval includes the blanket, structural wall and concrete shield. Free adiabatic boundary conditions were used. Initial distributions were uniform for all the parameters, except for internal energy, which was determined from neutronics

Table 1. Blanket structure and energy deposition in the zones.

Zone	Matter	Radius (cm)	Energy density (MJ m^{-3})	Temperature rise (K)
1	PbLi	400.0	23.8	13.0
2	SiC + PbLi	400.2	20.7	5.1
3	PbLi	401.0	18.5	11.1
4	V_4Cr_4Ti	407.0	8.9	2.8
5	PbLi	407.4	12.2	7.3
6	V_4Cr_4Ti	413.4	6.1	1.7
7	PbLi	413.8	6.5	4.0
8	V_4Cr_4Ti	419.8	2.8	0.9
9	PbLi	420.2	4.1	2.0
10	V_4Cr_4Ti	426.2	1.1	0.5
11	PbLi	426.6	1.5	0.9
12	V_4Cr_4Ti	432.6	0.8	0.2
13	PbLi	433.0	0.9	0.4
14	V_4Cr_4Ti	439.0	0.2	0.1
15	PbLi	439.4	0.3	0.2
16	V_4Cr_4Ti	445.4	0.1	0.05
17	HT-9	446.4	0.07	0.01
18	Concrete	452.0	—	—

Table 2. Properties of reactor chamber materials.

Parameter	LiPb	SiC + LiPb	VCrTi	HT-9	Concrete
ρ, kg m^{-3}	9500	4800	6100	7800	1600
K, GPa	35	81.5	280	158	20
G, GPa	0	55	42.7	77.6	17
Y, MPa	—	35	223	422	—
Γ	2.7	2	1.23	2	2
c, m s^{-1}	1922	4120	6780	4500	3535
C_p, J kg^{-1} K^{-1}	188	660	546	700	840
λ, W m^{-1} K^{-1}	16	10.9	34	33	1.28

computations. The data for solid materials, silicon carbide, vanadium alloy and stainless steel are given by Zinkle in [13]. The eutectic $Li_{17}Pb_{83}$ properties are taken from [14]. The equation of state is taken in the Mie–Gruneisen form. The Gruneisen coefficient Γ is projected as 2 for the SiC porous wall, stainless steel and concrete. The material properties are given in table 2.

In figure 8 the pressure radial distribution in the blanket and the structural wall is drawn for different times. The right

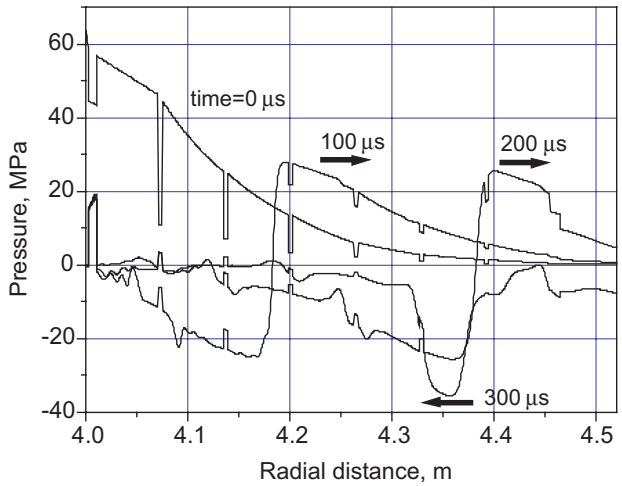

Figure 8. Pressure distribution in the FIHIF reactor chamber blanket and the structural wall at various times.

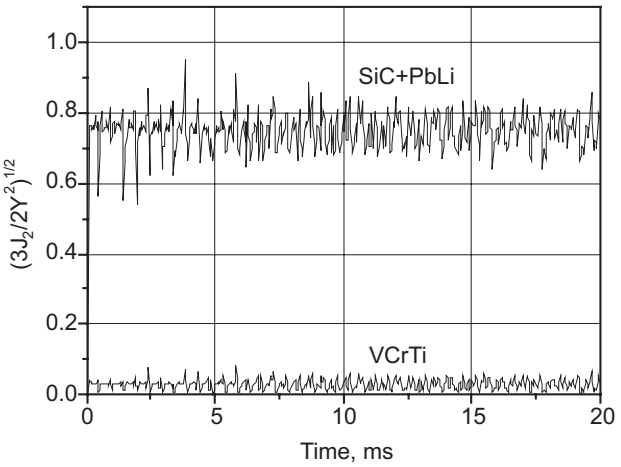

Figure 9. Temporal variation of equivalent stress normalized by yield stress Y ($Y = 35$ MPa for SiC/PbLi and 280 MPa for V–Cr–Ti). The von Mises criterion determines elastic/plastic material behaviour.

boundary is the contact interface between stainless steel and concrete.

The pressure distribution at $t = 0$ corresponds to instantaneous heating of the blanket. Monotonically decreasing parts of this curve belong to the PbLi coolant. Negative peaks of pressure are located in the blanket channel walls and reflect lower neutron absorption in SiC and V–Cr–Ti materials.

For $t > 0$, the compression release wave travels across the blanket. The velocity of the wave is equal to 2000 m s^{-1}. At $t = 250\,\mu$s the wave is refracted from the stainless steel–concrete contact surface and reflects back to the blanket as a tension wave. At the pressure profiles near the walls, relatively small perturbations are produced due to loading and release of the walls.

Thus, pulsations of pressure in the coolant and of stresses in walls are generated. In liquids these pulsations may cause cavitation effects.

In the walls, a control of stresses with respect to the strength material behaviour is needed. In figure 9 the equivalent stress $\sigma_e = (3J_2/2)^{1/2}$ normalized by the yield stress Y is plotted versus time for two construction walls: the first wall is SiC + PbLi and adjacent to it is the V–Cr–Ti wall.

Low and high frequency pulsations are seen. They are caused by the reflection of the main pulse and reverberation of walls, respectively.

The equivalent stress σ_e in the first wall is quite close to the yield stress Y, while in the vanadium alloy wall σ_e is substantially less than Y. According to the von Mises criterion $\sigma_e \leqslant Y$, both materials are in the elastic mode of loading.

4. Energy conversion and balance of plant system

The energy conversion system consists of three loops. The coolant of the second loop is sodium. The third loop is a steam turbine cycle. The key parameter of the system is the maximum temperature of $Li_{17}Pb_{83}$ at the outlet of the reactor chamber. It is taken as 823 K. The inlet temperature of the eutectic is equal to 623 K. The inlet and outlet temperatures of sodium in the intermediate heat exchanger are 573 K and 773 K, respectively.

Table 3. Parameters of thermal loops of FHIF power plant.

First loop	
Coolant	LiPb
Mass flow rate, kg s^{-1}	13 063
Pump power, kW	11 584
Second loop	
Coolant	Na
Mass flow rate, kg s^{-1}	6402
Pump power, kW	3768
Steam cycle	
Mass flow rate, kg s^{-1}	548.7
Inlet pressure, MPa	18
Superheat pressure, MPa	3
Condenser pressure, MPa	0.009
Turbine efficiency	0.875
Steam cycle efficiency	0.417
Reactor	
Fusion power, MW	1500
Driver power, MW	60
Neutron power ratio	0.773
Blanket multiplication	1.117
Power plant	
Thermal efficiency	0.407
Net efficiency	0.374
Net power output, MW	626

In table 3 the mass flow rate and the pump power for liquid metal coolants are given.

The steam cycle is configured with a reheat. The initial steam temperature and the reheat temperature are equal to 743 K. The temperature of feeding water is computed as 450 K. The efficiency of the steam cycle equals 0.407. Taking into account the driver efficiency, the target gain and the blanket multiplication for the fusion power of 1500 MW, we obtain the net efficiency of the plant to be 0.373 and net power per reactor of 626 MW.

5. Conclusions

The FIHIF concept, based on the high-energy ion beam drive of a cylindrical target, is characterized by new features in

the reactor chamber response to matter and energy fluxes, generated by DT microexplosions. Due to increased mass of the target shell the x-ray radiation has quite a long duration of several hundreds of nanoseconds and, in turn, a correspondingly smaller intensity.

However, hydrodynamic simulation of x-ray interaction with the first wall liquid film demonstrates shock generation in the film and a substantial recoil pulse, caused by expansion of ionized vapour.

The evaluation of mechanical loading of the first wall material shows that x-ray impact might be tolerable to the first wall. The problem in liquid film behaviour involves its fracture under loading conditions. This may result in droplets filling the reactor chamber cavity and the resulting complication of cavity clean-up.

The computation of the liquid film revaporization caused by reheating of vapour by ion debris and subsequent condensation shows that relaxation of the atmosphere of the reactor chamber to the initial conditions is fast enough (from 1 to 10 ms) in order to be a limiting factor for the repetition rate. The fast condensation of vapour is well accomplished, when an array of dispersed jets is employed in the reactor chamber.

The neutron transport 2D-computations determine the TBR (1.112) and blanket energy multiplication factor (1.117) and yield data on the thermal energy density distribution in the blanket design.

The blanket heating is very fast and occurs isochorically. This causes pressure/stress wave propagation across the blanket. The simulation of the wave processes in the blanket by means of a 1D strength mechanics code reveals the spectrum of pressure pulsations in the coolant and stress pulsation in tubing walls. Although the state of the first wall material stays in the elastic mode, the problems of concern are the determination of material fatigue under cycling loading and material strength deterioration under neutron irradiation. An additional problem of concern may arise due to cavitation effect in the coolant at negative pressures.

Acknowledgments

This work is sponsored by the Human Capital Foundation under contract N32. It is supported in part by the Complex Program on Basic Research of the Presidium of Russian Academy of Sciences N17.

References

[1] Lindl J.D. *et al* 2003 *Plasma Phys. Control. Fusion* **45** A217
[2] Meier W.R. *et al* 2003 *Fusion Eng. Des.* **62–63** 577
[3] Medin S.A. *et al* 2002 *Laser Part. Beams* **20** 419
[4] Medin S.A. *et al* 2003 *Fusion Sci. Technol.* **43** 437
[5] Basko M.M. *et al* 2002 *Laser Part. Beams* **20** 411
[6] Moir R.W. 1996 *Fusion Eng. Des.* **32–33** 93
[7] Hubbell J.H. and Seltzer S.M. 1996 *Tables of X-Ray Mass Attenuation Coefficients* (NIST)
[8] Medvedev A.B. 2004 Modification of the van der Waals model for dense states of matter *High Pressure Shock Compression of Solids VII, Shock Waves and Extreme States of Matter* ed V.E. Fortov *et al* (New York: Springer) chapter 13, p 531
[9] Bohachevsky I.O. 1979 Fusion impulse containment *Proc. Impact Fusion Workshop (LASL, Los Alamos, July 1979)* p 83
[10] Rossi B. 1952 *High Energy Particles* (Englewood Cliffs, NJ: Prentice-Hall)
[11] Isachenko V.P. 1977 *Heat Transfer in Condensation Processes* (Moscow: Energia) (in Russian)
[12] GROUP-6 1981 MCNP—A General Monte Carlo Code for Neutron and Photon Transport, LA-7396-m revised, Los Alamos National Laboratory
[13] Zinkle S.J. 1998 Status of recent activities by the APEX material group *APEX Study Meeting* Sundia National Laboratories, p 18
[14] Mikhailov V.N. *et al* 1999 *Lithium in Fusion and Space Power in 21st Century* (Moscow: Nauka) (in Russian)